May 2005

Analysis of sedimentation biodetectors

Shizhi Qian
University of Pennsylvania

Raimund Bürger
University of Stuttgart Pfaffenwaldring

Haim H. Bau
University of Pennsylvania, bau@seas.upenn.edu

Postprint version. Published in *Chemical Engineering Science*, Volume 60, Issue 10, May 2005, pages 2585-2598.
Publisher URL: http://dx.doi.org/10.1016/j.ces.2004.12.014

Analysis of sedimentation biodetectors

Abstract
A bead-based sedimentation biodetector is studied theoretically. The biodetector operates with a suspension of settling beads, non-settling reporters, and target analytes – all initially suspended in a buffer solution. The reporters can be either fluorescent molecules or small particles. The functionalized beads interact with the reporters and target analytes while settling under the action of gravitational, electric, and/or magnetic fields. Both sandwich and competitive assays with hindered settling are considered. In the sandwich format, in the presence of target analytes, the reporters bind to the beads and settle (the target analytes provide the link between the beads and the reporters). A reduction in the reporters' concentration indicates the presence of target analytes. In the competitive format, both target analytes and reporters compete for bead-based binding sites. In the absence of target analytes, one would observe a reduction in the suspended reporters' concentration. The model allows one to predict the reporters' concentration in solution as a function of initial bead, reporter, and target analyte concentrations and provides a means for the reactor's optimization.

Keywords
sedimentation, biodetector, competitive assay, sandwich assay

Comments
Postprint version. Published in *Chemical Engineering Science*, Volume 60, Issue 10, May 2005, pages 2585-2598.
Publisher URL: http://dx.doi.org/10.1016/j.ces.2004.12.014

Qian, S. Burger, R., and Bau, H., H., 2005, Analysis of Sedimentation Biodetectors, Chemical Engineering Science, 60, 2585 – 2598

Analysis of Sedimentation Biodetectors

Shizhi Qian[a], Raimund Bürger[b], Haim H. Bau[a+]

[a]Mechanical Engineering and Applied Mechanics, University of Pennsylvania

Philadelphia, PA 19104, USA

[b]Institute of Applied Analysis and Numerical Simulation, University of Stuttgart
Pfaffenwaldring 57, D-70569 Stuttgart, Germany

ABSTRACT

A bead-based sedimentation biodetector is studied theoretically. The biodetector operates with a suspension of settling beads, non-settling reporters, and target analytes – all initially suspended in a buffer solution. The reporters can be either fluorescent molecules or small particles. The functionalized beads interact with the reporters and target analytes while settling under the action of gravitational, electric, and/or magnetic fields. Both sandwich and competitive assays with hindered settling are considered. In the sandwich format, in the presence of target analytes, the reporters bind to the beads and settle (the target analytes provide the link between the beads and the reporters). A reduction in the reporters' concentration indicates the presence of target analytes. In the competitive format, both target analytes and reporters compete for bead-based binding sites. In the absence of target analytes, one would observe a reduction in the suspended reporters' concentration. The model allows one to predict the reporters' concentration in solution as a function of initial bead, reporter, and target analyte concentrations and provides a means for the reactor's optimization.

Keywords: Sedimentation, Biodetector, Competitive assay, Sandwich assay

1. Introduction

[+] Corresponding author
E-mail addresses: shizhi@seas.upenn.edu (S. Qian), buerger@mathematik.uni-stuttgart.de (R. Bürger), bau@seas.upenn.edu (H. H. Bau)

In recent years, there has been a growing interest in developing low-cost techniques for inexpensive, rapid identification of various pathogens at the point of care. For example, the lateral flow immunoassay is a popular diagnostic tool because it eliminates the need for trained personnel and expensive equipment and provides rapid diagnostics at the point of care (Qian and Bau, 2003, 2004). The lateral flow immunoassay consists of a nitrocellulose membrane in which reporter particles and target analytes are propelled to an interaction zone by capillary forces. Unfortunately, relatively large membrane-to-membrane variations, the adhesion of reporter particles and target analytes to the membrane, and the presence of significant background noise reduce the sensitivity of this format.

An interesting alternative is the sedimentation reactor (Lim, 1990; Lim and Ko, 1990; Lim et al., 1998; House et al., 2001; Oracz et al., 2003; Tam et al., 2003; Feleszko et al., 2004). The sedimentation assay consists of functionalized beads (B), functionalized reporter particles (P), and target analytes (A). The beads are typically much larger and tend to settle much faster than the reporter particles. The latter can stay in solution for a very long time. The settling process can be accelerated with the use of centrifugal forces or magnetic fields (when the beads are made of a magnetic material). The reporter particles may consist of colored particles, fluorescent labels, magnetic materials, or phosphor particles. The detection technique is dictated by the nature of the reporter particles. For example, colored particles can be detected visually while phosphor particles are typically excited with a laser and their emission is measured with a photo-detector. Two different assays are possible: sandwich and competitive.

In the sandwich format, the target analyte (A) binds to both the beads (B) and the reporter particles (P) to form the complexes BA and AP. The complex BA can bind with P or the complex AP can bind with B to form the sandwich complex BAP. The beads and their complexes settle to the bottom of the reactor while the free target analytes and reporter particles remain in solution. Figs. 1a and b sketch, respectively, the processes in the absence and presence of target analytes. In the absence of or at low concentrations of target analyte (A), the reporter

particles (P) cannot bind to the heavier settling beads (B). They remain suspended, and there is no change in the supernatant's color or signal intensity. In the presence of target analytes, some of the reporter particles bind to the beads and settle. This leads to a reduction in the supernatant's signal. As the target analyte concentration increases, the supernatant's signal intensity decreases.

In the competitive format, the target analyte (A) and the functionalized reporter particles (P) can competitively bind to the functionalized heavier beads (B) as they settle to the bottom of the reactor. When the analyte (A) is absent, most of the reporter particles bind to the beads, and there is an obvious color change in the supernatant. When there is an abundance of target analytes, the target molecules occupy many of the binding sites on the beads, and most of the reporter particles remain in solution. Hence, little or no change in the supernatant's color indicates the presence of an abundance of target analytes. Figs. 2a and 2b depict the competitive process in the absence and the presence of target analytes, respectively. The TUBEX^{TM} (IDL Biotech, Sollentuna, Sweden) used to detect anti-O9 (immunoglobulin M (IgM) mouse hybridoma) antibodies is an example of a sedimentation reactor operating with a competitive assay (Lim, 1990; Lim and Ko, 1990; Lim et al., 1998; House et al., 2001; Oracz et al., 2003; Tam et al., 2003; Feleszko et al., 2004). In this immunoassay, colored latex particles coated with anti-O9 mAb and magnetic particles coated with Salmonella *typhi* LPS are mixed in a tube with the sample to be examined. Subsequently, the reactor tube is placed on a magnet, and the magnetic beads settle to the bottom of the tube. The detection results are based on the concentration of the indicator particles that remain suspended as indicated by the color of the supernatant.

The designers of bioassays typically employ empirical means to optimize the assay format (i.e., the selection of the optimal bead and reporter particle concentrations needed to achieve high sensitivity at pre-specified target analyte concentrations). It appears that it would be desirable to have a predictive tool that can provide quantitative information. To the best of our knowledge, such a mathematical model accounting for the effects of hindered settling has

not been developed. This paper takes a few, first steps in the development of such a modeling tool.

Sedimentation of polydisperse suspensions of solid particles with different sizes and densities are widely used in unit operations; materials, minerals, food, and pharmaceuticals processing; and wastewater treatment (Sharma et al., 1993; Concha and Bürger, 2002; Berres et al., 2003; Xue and Sun, 2003). Bürger and Wendland (2001) and Concha and Bürger (2002) review sedimentation research with a focus on mineral processing. Several mathematical models, based on multiphase flow theory for the sedimentation of monodisperse or polydisperse suspensions, with and without considering sediment compressibility, have also been proposed (Smith, 1965, 1966; Lockett and Al-Habbooby, 1973; Mirza and Richardson, 1979; Masliyah, 1979; Lockett and Bassoon, 1979; Batchelor, 1982; Batchelor and Wen, 1982; Selim et al., 1983; Shih et al., 1987; Davis and Gecol, 1994; Bürger and Tory, 2000; Bürger et al., 2000a, 2000b, 2000c, 2001, 2002; Xue and Sun, 2003; Berres et al., 2003, 2004a, 2004b; Tory and Ford, 2004). The predictions of the mathematical models, solved numerically by recently developed finite difference schemes for conservation laws under various batch and continuous flow conditions, favorably agree with experiments (Berres et al., 2003, 2004a, 2004b, 2005; Xue and Sun, 2003; Bürger et al., 2000c; Bürger et al., 2001; Zeidan et al., 2004). A simpler Lamm equation has also been used in the analysis of centrifugal sedimentation reactors (Schuck, 1998, 2004a, 2004b, and the references cited therein, and Stafford and Braswell, 2004). In fact, the Lamm equation is a simpler variant of the multiphase flow models, and it neglects the effect of hindered settling and includes diffusion terms that ensure that the solutions of the equations are smooth. However, hindered settling is important, especially when the solid volume fraction is great enough to inhibit liquid movement and liquid must move in the spaces between particles. Yet none of the existing models accounts for chemical reactions and biological interactions with hindered settling that may occur during the sedimentation process of polydisperse suspension. The

objective of this paper is to propose such a model, which would be useful for the design and optimization of sedimentation biodetectors working with competitive and sandwich assays.

The paper is organized in the following way. Sections 2 and 3 extend, respectively, the Masliyah-Lockett-Bassoon (MLB) model (Masliyah, 1979; Lockett and Bassoon, 1979) as described by Bürger et al (2002) and the high-resolution Kurganov-Tadmor central-difference scheme (Kurganov and Tadmor, 2000) to account for biological interactions. The presence of shocks requires the use of a shock-capturing scheme. Section 4 provides a few examples of the calculations, and section 5 concludes. Unfortunately, we were not able to find any quantitative experimental data to compare with our calculations.

2. Mathematical Model

Consider an upright cylindrical sedimentation reactor of height L, initially filled with a homogeneous suspension of N_s species of protein-conjugated particles, (N_f-1) target analytes, and a buffer solution. In total, the solution consists of $N=N_s+N_f$ species. The target analytes are assumed to be present at very low concentrations, to have a negligible effect on the buffer solution's density and viscosity, and to translate at the velocity of the buffer. In contrast, the particle species have a significant effect on the solution's properties and move at velocities different than the surrounding buffer. We describe the suspension as a superposition of continua (Drew and Passman, 1999). Both the liquid and solid media are treated as viscous fluids. The model presented here is an extension of the treatment given in Bürger et al (2002).

2.1 Mass and Linear Momentum Balance Equations

In this section, we formulate the mass and momentum conservation equations. We consider the target analytes and the buffer to be a single phase. By definition, the volume fractions $\phi_j \quad (j = 1,..., N_s)$ of all the solid phases and the liquid sum up to one:

$$\sum_{j=1}^{N_s+1}\phi_j = 1, \tag{1}$$

where $\phi = \phi_1 + \ldots + \phi_{N_s}$ is the total volume fraction occupied by all solid particle species and $\phi_{N_s+1} = 1-\phi$ is the volume fraction of the fluid phase. We define a vector $\mathbf{\Phi} = \left(\phi_1,\ldots,\phi_{N_s}\right)^T$ for later use. Hereafter, bold letters denote vectors.

The continuity equation for each solid phase is

$$\frac{\partial \rho_i \phi_i}{\partial t} + \nabla\cdot(\rho_i\phi_i\mathbf{v}_i) = m_i^s, \qquad i = 1,...,N_s \tag{2}$$

where $\mathbf{v}_i$ is the i^{th} solid phase velocity vector, m_i^s is the rate of production of the i^{th} solid phase, and ρ_i is the (constant) density of the i^{th} solid phase. Both the liquid and solid phases are incompressible. The first term on the left hand side of equation (2) accounts for the rate of mass accumulation per unit volume, and the second term is the net rate of convective mass flux. The term on the right accounts for the interphase mass transfer resulting from biological interactions. We neglect mass transport due to diffusion.

The continuity equation of each species in the fluid phase is:

$$\frac{\partial \rho_f \phi_{N_s+1} Y_i}{\partial t} + \nabla\cdot(\rho_f\phi_{N_s+1}Y_i\mathbf{v}_f) = m_i^f, \quad i = 1,...,N_{\mathrm{f}} \tag{3}$$

where $\mathbf{v}_f$ is the fluid phase's velocity; ρ_f is the density of the fluid phase; and m_i^f and Y_i are, respectively, the rate of production and the mass fraction of the i^{th} species in the fluid phase. By definition,

$$\sum_{i=1}^{N_f} Y_i = 1. \tag{4}$$

We define the vector $\mathbf{X} = (X_1,\ldots,X_{N_f})^T$, where $\mathrm{X}_i = \phi_{N_s+1}Y_i = (1-\phi)Y_i$ and $\sum_{i=1}^{N_f} X_i = (1-\phi)$. Equation (3) can be expressed in terms of X_i as:

$$\frac{\partial X_i}{\partial t} + \nabla\cdot(X_i\mathbf{v}_f) = \frac{m_i^f}{\rho_f}, \; i = 1,...,N_{\mathrm{f}}. \tag{5}$$

Conservation of mass requires that the net mass transfer over all phases must be zero,

$$\sum_{i=1}^{N_s} m_i^s + \sum_{i=1}^{N_f} m_i^f = 0. \tag{6}$$

Summing up the individual equations (5), we have

$$-\frac{\partial \phi}{\partial t} + \nabla \cdot [(1-\phi)\mathbf{v}_f] = \frac{1}{\rho_f} \sum_{i=1}^{N_f} m_i^f. \tag{7}$$

The volume-average velocity of the suspension is:

$$\mathbf{q} := (1-\phi)\mathbf{v}_f + \sum_{i=1}^{N_s} \phi_i \mathbf{v}_i \ . \tag{8}$$

Dividing the *i*-th equation in (2) by ρ_i, summing the resulting equations over $i=1,\ldots,N_s$, adding the result to equation (7), and using the constraint (6), we obtain:

$$\nabla \cdot \mathbf{q} = \sum_{i=1}^{N_s} m_i^s \left(\frac{1}{\rho_i} - \frac{1}{\rho_f} \right). \tag{9}$$

The momentum equation for each solid phase is:

$$\rho_i \phi_i \left[\frac{\partial \mathbf{v}_i}{\partial t} + (\mathbf{v}_i \cdot \nabla)\mathbf{v}_i \right] = -\nabla(\phi_i p) + \nabla \cdot \overline{\overline{T}}_i^V + \rho_i \phi_i \mathbf{b} + \mathbf{I}_i^f + \sum_{\substack{k=1 \\ k \neq i}}^{N_s} \mathbf{I}_i^k + m_i^s \mathbf{v}_i, \ i = 1,\ldots,N_s \tag{10}$$

where p is the pressure; $\overline{\overline{T}}_i^V$ is the viscous part of the stress tensor of the i^{th} particle species (the particle species are treated as pseudofluids); $\mathbf{b}$ is the body force density; $\mathbf{I}_i^f$ is the interaction force representing the momentum transfer between the i^{th} particle species and the fluid phase; $\mathbf{I}_i^k$ is the interaction force between the i^{th} and k^{th} particle species; and $m_i^s \mathbf{v}_i$ describes the momentum transfer associated with the mass transfer.

Similarly, the momentum equation for the fluid phase is:

$$\rho_f (1-\phi) \left[\frac{\partial \mathbf{v}_f}{\partial t} + (\mathbf{v}_f \cdot \nabla)\mathbf{v}_f \right] = \nabla((1-\phi)p) + \nabla \cdot \overline{\overline{T}}_f^V + \rho_f (1-\phi)\mathbf{b} - \sum_{i=1}^{N_s} \mathbf{I}_i^f + \sum_{i=1}^{N_f} m_i^f \mathbf{v}_f \ . \tag{11}$$

The terms on the right hand side of equation (11) represent, respectively, the pressure, the viscous part of the fluid phase stress tensor, the body force, the interaction forces between the

fluid phase and all solid phases, and the momentum transfer due to biological interactions of all the species in the fluid phase.

Although the model can accommodate body forces resulting from magnetic, electrical, and centrifugal forces, we will consider here only the case of the gravitational force $\mathbf{b} = -g\hat{\mathbf{k}}$, where $\hat{\mathbf{k}}$ is the upward-pointing unit vector.

2.2 Interaction Forces

The interaction force between the fluid and the i^{th} solid species is modeled by

$$\mathbf{I}_i^f = \alpha_i(\mathbf{\Phi})\mathbf{u}_i + p\nabla\phi_i, \qquad i = 1,...,N_s \tag{12}$$

where $\mathbf{u}_i = \mathbf{v}_i - \mathbf{v}_f$ is the slip velocity of the particle species *i*, and $\alpha_i(\mathbf{\Phi})$ is the resistance coefficient (Bürger et al., 2002)

$$\frac{\phi_i}{\alpha_i(\mathbf{\Phi})} = -\frac{d_i^2 V(\phi)}{18\mu_f}; \tag{13}$$

μ_f is the viscosity of the fluid;

$$V(\phi) = \begin{cases} (1-\phi)^{n-2} & (\text{n} > 2) \qquad \text{for} \quad 0 \le \phi \le \phi_{\max} \\ 0 & \text{otherwise} \end{cases}, \tag{14}$$

is the hindered settling factor (Richardson and Zaki, 1954); and $\phi_{\max}$ is the volume fraction of the settled particles.

The interactions among the different solid particle species could be specified by the Nakamura and Capes formula (Nakamura and Capes, 1976; Arastoopour et al., 1982; Shih et al., 1987; Bürger et al., 2002). Since these interaction forces can be neglected in our case (see section 2.4), we do not reproduce the explicit expressions here.

Introducing relationship (12) into the momentum equations, we obtain, respectively, the modified momentum equations for the solid and fluid phases:

$$\rho_i\phi_i\left[\frac{\partial \mathbf{v}_i}{\partial t}+\left(\mathbf{v}_i\cdot\nabla\right)\mathbf{v}_i\right]=-\phi_i\nabla p+\nabla\cdot\overline{\overline{T}}_i^{V}+\rho_i\phi_i\mathbf{b}+\alpha_i(\mathbf{\Phi})\mathbf{u}_i+\sum_{\substack{k=1\\k\neq i}}^{N_s}\mathbf{I}_i^k+m_i^s\mathbf{v}_i,\ i=1,...,N_s \tag{15}$$

and

$$\rho_f(1-\phi)\left[\frac{\partial \mathbf{v}_f}{\partial t}+(\mathbf{v}_f\cdot\nabla)\mathbf{v}_f\right]=-(1-\phi)\nabla p+\nabla\cdot\overline{\overline{T}}_f^{V}+\rho_f(1-\phi)\mathbf{b}-\sum_{i=1}^{N_s}\alpha_i(\mathbf{\Phi})\mathbf{u}_i-\sum_{i=1}^{N_s}m_i^s\mathbf{v}_f. \tag{16}$$

2.3 Mass Transfer Due to Biological Interactions

The rates of mass production, $m_1^s,\ldots,m_{N_s}^s$ and $m_1^f,\ldots,m_{N_f}^f$, are the result of the biological interactions that occur during the sedimentation process. Since the concentrations of the particles and target analytes are very low, we assume reversible, 1:1 interactions:

$$C_{a(i)}+C_{b(i)}\underset{k_d^i}{\overset{k_a^i}{\Leftrightarrow}}C_{c(i)},\qquad i=1,...,R \tag{17}$$

In other words, the binding of multiple target analytes and/or reporter particles to a single bead is a low probability event. In the above, *R* is the total number of possible interactions; k_a^i and k_d^i are, respectively, the association and dissociation rate constants of the i^{th} interaction; and $C_{a(i)}$, $C_{b(i)}$ and $C_{c(i)}$ denote the various species involved in the i^{th} interaction, each of which corresponds to one of the particles or fluid species. The rate of formation of the j^{th} species is:

$$[C_j']=\sum_{i=1}^{R}\left\{k_a^i\left(\delta_{j,c(i)}-\delta_{j,a(i)}-\delta_{j,b(i)}\right)[C_{a(i)}][C_{b(i)}]-k_d^i\left(\delta_{j,c(i)}-\delta_{j,a(i)}-\delta_{j,b(i)}\right)[C_{c(i)}]\right\},\ j=1,...,N \tag{18}$$

where the square brackets [ ] denote molar concentration; $X'=dX/dt$; and $\delta_{i,j}$ is the Kronecker delta ($\delta_{i,j}=1$ when $i=j$ and $\delta_{i,j}=0$ when $i\neq j$). The "molar" concentration of the solid particles is the ratio of the number of particles per liter divided by the Avogadro number. The molar concentration of the target molecules has its usual meaning $[C_i]=\rho_f X_i/MW_i$,

where MW_i is the molecular mass of the i^{th} species. When we consider particles, $[C_i] = \rho_s \phi_i / MW_i$ and MW_i is the mass of individual particles.

The rate of mass transfer vector,

$$\mathbf{m} = (m_1, \ldots, m_N)^T = (m_1^s, \ldots, m_{N_s}^s, m_1^f, \ldots m_{N_f}^f)^T,$$

where

$$m_i(\mathbf{W}) = MW_i[C_i'], \quad i = 1,...,N \tag{19}$$

is a function of the vector

$$\mathbf{W} = (W_1, ..., W_{N_s}, W_{N_s+1}, \ldots, W_N)^T = (\phi_1, ..., \phi_{N_s}, X_1, \ldots, X_{N_f})^T. \tag{20}$$

2.4 Order of Magnitude Estimates

The momentum equations for the solid (15) and fluid (16) phases are quite complicated. Fortunately, order of magnitude analysis allows one to demonstrate that certain terms are unimportant and that the equations can be significantly simplified (Bürger et al., 2002; Berres et al., 2003). We use ρ_f as the density scale; the velocity U of the fastest settling particle in an unbounded medium as the velocity scale; the height of the device L as the length scale; the settling time L/U as the time scale; and the hydrostatic pressure $\rho_f gL$ as the pressure scale. The representative kinematic viscosities of the solid and fluid phases are denoted, v_0^s and v_0^f, respectively. The dimensionless momentum equations for the solid phases and the liquid are, respectively,

$$\rho_i^* \phi_i Fr \frac{D\mathbf{v}_i^*}{Dt^*} = -\phi_i \nabla^* p^* + \frac{d_1}{L}\frac{v_0^s}{v_0^f}\frac{Fr}{\mathrm{Re}}\nabla^* \cdot (\overline{\overline{T}}_i^V)^* - \rho_i^* \phi_i \hat{\mathbf{k}} + \alpha_i^*(\mathbf{\Phi})\mathbf{u}_i^* + \frac{L}{d_1} Fr \sum_{\substack{k=1 \\ k \neq i}}^{N_s} \left(\mathbf{I}_i^k\right)^* + \frac{m_i^s U}{\rho_f g}\mathbf{v}_i^*, \qquad i = 1,..., N_s \tag{21}$$

and

$$\nabla^* p^* = -\hat{\mathbf{k}} - \frac{1}{(1-\phi)}\sum_{i=1}^{N_s}\alpha_i^*(\mathbf{\Phi})\mathbf{u}_i^* - \mathrm{Fr}\frac{D\mathbf{v}_f^*}{Dt^*} + \frac{1}{(1-\phi)}\frac{d_1}{L}\frac{\mathrm{Fr}}{\mathrm{Re}}\nabla^*\cdot(\overline{\overline{T}}_f)^* - \frac{U}{\rho_f g(1-\phi)}\sum_{i=1}^{N_s} m_i^s \mathbf{v}_f^* \quad . \tag{22}$$

In the above, the superscript star denotes dimensionless quantities. The Froude number $Fr = U^2/(gL)$ is proportional to the ratio of kinetic and potential energies. The sedimentation Reynolds number $\mathrm{Re} = Ud_1/\nu_0^f$ is the ratio between inertial and viscous forces, and d_1 is the diameter of the largest particle.

In our application, the size of the largest particle d_1~10^{-6}m, the height of the settling vessel L~10^{-1} m, g~10m^2/s, ρ_f =10^3kg/m^3, and ν_0^f =10^{-6} m^2/s. Based on the Stokes velocity, we estimate U~10^{-5}m/s. Accordingly, Fr=10^{-10}, Re=10^{-5}, and d_1/L=10^{-5}. It is also reasonable to assume that $\nu_0^s << \nu_0^f$ (Bürger et al., 2002). The maximum rate of the interactions occurs when no complexes are present. Typical initial concentrations of the free (unbound) particles and target analytes are on the order of 10^{-8}M. The association rate constants are $O(10^7\mathrm{M}^{-1}\mathrm{s}^{-1})$ and the molecular masses are $O(10^{11}$kg/mol). Consequently, $m_i^s U/\rho_f g \sim k_a[C_0]^2 \times MW \times U/(\rho_f g) = 10^{-7}$. Lastly, numerous experimental and theoretical studies have demonstrated that the interactions among the solid phases can be neglected at the very low Reynolds number considered here (Bürger et al., 2002). Assuming that all the dimensionless variables are $O(1)$ and discarding terms that have coefficients of $O(10^{-5})$ or smaller, we obtain the simplified momentum equations for the solid and fluid phases:

$$0 = -\phi_i\nabla^* p^* - \rho_i^*\phi_i\hat{\mathbf{k}} + \alpha_i^*(\mathbf{\Phi})\mathbf{u}_i^*, \quad i = 1,..., N_s \tag{23}$$

and

$$\nabla^* p^* = -\hat{\mathbf{k}} - \frac{1}{(1-\phi)}\sum_{i=1}^{N_s}\alpha_i^*(\mathbf{\Phi})\mathbf{u}_i^* . \tag{24}$$

Equations (23) and (24) rewritten in dimensional form are:

$$\alpha_i(\mathbf{\Phi})\mathbf{u}_i = \rho_i\phi_i g\hat{\mathbf{k}} + \phi_i\nabla p,\ i=1,...,N_s \tag{25}$$

and

$$\nabla p = -\rho_f g\hat{\mathbf{k}} - \frac{1}{(1-\phi)}\sum_{i=1}^{N_s}\alpha_i(\mathbf{\Phi})\mathbf{u}_i\,. \tag{26}$$

Inserting equation (26) into equation (25) to eliminate the pressure *p* and solving explicitly for the slip velocities $\mathbf{u}_1,...,\mathbf{u}_{N_s}$ with the Sherman-Morrison formula (Bürger et al., 2002), we get

$$\mathbf{u}_i = \mu\delta_i\left(\overline{\rho}_i - \sum_{j=1}^{N_s}\overline{\rho}_j\phi_j\right)V(\phi)\hat{\mathbf{k}}, \qquad i=1,...,N_s \tag{27}$$

where $\delta_i = d_i^2/d_1^2$, $\mu = -gd_1^2/(18\mu_f)$, $\overline{\rho}_i = \rho_i - \rho_f$.

2.5 Simplified Mathematical Model

The simplified mathematical model consists of the equations:

$$\frac{\partial\phi_i}{\partial t} + \nabla\cdot[\phi_i\mathbf{q} + f_i(\mathbf{\Phi})\hat{\mathbf{k}}] = \frac{m_i^s}{\rho_i}, \qquad i=1,...,N_s \tag{28}$$

$$\frac{\partial X_i}{\partial t} + \nabla\cdot\left[X_i\mathbf{q} - \frac{X_i}{1-\phi}\sum_{j=1}^{N_s}f_j(\mathbf{\Phi})\hat{\mathbf{k}}\right] = \frac{m_i^f}{\rho_f}, \quad i=1,...,N_f \tag{29}$$

and

$$\nabla\cdot\mathbf{q} = \sum_{i=1}^{N_s}m_i^s\left(\frac{1}{\rho_i} - \frac{1}{\rho_f}\right), \tag{30}$$

where

$$f_i(\mathbf{\Phi}) = \mu V(\phi)\phi_i\left[\delta_i\left(\overline{\rho}_i - \sum_{j=1}^{N_s}\overline{\rho}_j\phi_j\right) - \sum_{j=1}^{N_s}\delta_j\phi_j\left(\overline{\rho}_j - \sum_{k=1}^{N_s}\overline{\rho}_k\phi_k\right)\right], \quad i=1,...,N_s \tag{31}$$

In contrast to the previously studied models of sedimentation without reactions (Selim et al., 1983; Bürger and Tory, 2000; Bürger et al., 2002), the right hand sides of equations (28)-(30) are not zero. Moreover, in the proposed model, the sedimentation rate of each particle

species is concentration-dependent. This concentration dependence enters implicitly through the species' volume fraction.

2.6 One-Dimensional Model

We will focus on only one space dimension ($0 \le x \le L$) that is aligned along the height of the reactor. For a one-dimensional, closed, batch reactor, the mathematical model (28)-(30) simplifies to the hyperbolic system of equations:

$$\frac{\partial \mathbf{W}}{\partial t} + \frac{\partial}{\partial x}\mathbf{F}\left(\mathbf{W}, q(\mathbf{W})\right) = \mathbf{S}(\mathbf{W}) \,, \tag{32}$$

where $\mathbf{W} = (\mathbf{\Phi}, X_1, \ldots, X_{N_f})^T$ is the vector of the sought volume fractions; $\mathbf{F}\left(\mathbf{W}, q(\mathbf{W})\right) = (F_1, ..., F_N)^T$ is the flux vector,

$$F_i\left(\mathbf{W}, q(\mathbf{W})\right) = \begin{cases} W_i q + f_i(\mathbf{\Phi}) & \text{for } i = 1, \ldots, N_s \\ W_i\left[q - \dfrac{1}{1-\phi}\displaystyle\sum_{j=1}^{N_s} f_j(\mathbf{\Phi})\right] & \text{for } i = N_s + 1, ..., N \end{cases} ; \tag{33}$$

$\mathbf{S}(\mathbf{W}) = (S_1, ..., S_N)^T$ is the source vector; and

$$S_i = \begin{cases} m_i(\mathbf{W})/\rho_i & \text{for } i = 1, \ldots, N_s \\ m_i(\mathbf{W})/\rho_f & \text{for } i = N_s + 1, ..., N \end{cases} \tag{34}$$

Since neither particles nor liquid enter ($x=L$) or leave the column ($x=0$), we can state the boundary conditions:

$$\mathbf{F}\left(\mathbf{W}, q\right)\big|_{x=0} = \mathbf{F}\left(\mathbf{W}, q\right)\big|_{x=\mathrm{L}} = 0 \,. \tag{35}$$

At time t=0, the distribution of the volume fraction vector is $\mathbf{W}^0(x)$.

The one-dimensional version of equation (30),

$$\frac{\partial q}{\partial x} = \sum_{i=1}^{N_s} m_i^s \left(\frac{1}{\rho_i} - \frac{1}{\rho_f}\right), \tag{36}$$

is integrated to give

$$q(x,t) = q(0,t) + \int_0^x \frac{\partial q(\xi,t)}{\partial \xi} d\xi = \int_0^x \sum_{i=1}^{N_s} m_i^s\left(\mathbf{\Phi}(\xi,t)\right)\left(\frac{1}{\rho_i} - \frac{1}{\rho_f}\right) d\xi = \int_0^x \tilde{m}\left(\mathbf{\Phi}(\xi,t)\right) d\xi, \qquad (37)$$

where $q(0,t) = 0$, and

$$\tilde{m}\left(\mathbf{\Phi}\right) = \sum_{i=1}^{N_s} m_i^s\left(\mathbf{\Phi}\right)\left(\frac{1}{\rho_i} - \frac{1}{\rho_f}\right). \qquad (38)$$

3. **Numerical Scheme for One Dimensional Simulation**

The difficulty in solving equations (32) stems from the presence of discontinuities in the concentrations of the different particle species (Bürger et al., 2001). Here, we use an extended version of the explicit Kurganov-Tadmor central difference scheme (Kurganov and Tadmor, 2000). This scheme has the advantage of high resolution and low numerical (artificial) viscosity. Unfortunately, like all explicit schemes in conservation form, it requires small time-steps to assure numerical stability.

We divide the computational domain $Q_T=[0, L]\times[0, T]$ into the uniform grid in space and time. $x_j=j\Delta x$, $(j=0,\ldots,J)$, where J is an even integer and $\Delta x=L/J$, $\Delta t=T/N_T$, and $t_n=n\Delta t$, $(n=0,\ldots,N_T)$. The approximate cell averages of $W_1,\ldots,W_N$ with respect to the cell $[x_{j-1}, x_{j+1}]$ at time t_n are denoted $\overline{W}_{i,j}^{\,n}$:

$$\overline{W}_{i,j}^{\,n} := \frac{1}{2\Delta x}\int_{x_{j-1}}^{x_{j+1}} W_i^{\,n}(\xi)\, d\xi, \qquad j = 1,\ 3,...,J-1; \quad i = 1,\ 2,...,N \qquad (39)$$

We define the vector $\overline{\mathbf{W}}_j^n = (\overline{W}_{1,j}^n,\ldots,\overline{W}_{N,j}^n)^T$ for $j=1, 3,\ldots, J-1$ and $n=0, 1,\ldots,N_T$. For interior cells, the iterative scheme is of the form:

$$\overline{\mathbf{W}}_j^{n+1} = \overline{\mathbf{W}}_j^n - \lambda(\mathbf{h}_{j+1}^n - \mathbf{h}_{j-1}^n) + \Delta t\mathbf{S}_j^n, \qquad j = 3,5,...,J-3; \quad n = 0,1,...,N_T \qquad (40)$$

where $\lambda = \Delta t/(2\Delta x)$. The quantities $\mathbf{h}_{j\pm1}^n$ are the approximations of the "hyperbolic" flux $\mathbf{F}(\mathbf{W},q)$ through the boundaries of the cell $I_j:=[x_{j-1}, x_{j+1}]$ at time t_n. $\mathbf{S}_j^n$ is the discretization of

the source term associated with the cell I_j at time t_n. The detailed computation of $\mathbf{h}_{j\pm1}^n$ and $\mathbf{S}_j^n$ are deferred to the Appendix.

The discrete version of the boundary condition (35) is:

$$\mathbf{h}_0^n = 0 \quad \text{and} \quad \mathbf{h}_J^n = 0\,, \quad n = 0,...,N_T \tag{41}$$

Inserting (41) into (40), we obtain the boundary scheme:

$$\overline{\mathbf{W}}_1^{n+1} = \overline{\mathbf{W}}_1^n - \lambda \mathbf{h}_2^n + \Delta t \mathbf{S}_1^n, \quad n = 0,1,...,N_T \tag{42}$$

and

$$\overline{\mathbf{W}}_{J-1}^{n+1} = \overline{\mathbf{W}}_{J-1}^n + \lambda \mathbf{h}_{J-2}^n + \Delta t \mathbf{S}_{J-1}^n, \quad n = 0,1,...,N_T \tag{43}$$

For additional details of the numerical scheme, see the appendix.

The code was verified by comparing its predictions with documented calculations (Bürger et al., 2000c and 2001; Xue and Sun, 2003; Berres et al., 2003 and 2004a) and experiments of sedimentation in the absence of biological interaction.

4. Competitive Assay Sedimentation Biodetector

The suspension contains a mixture of reporter particles (P), settling beads (B), target analyte (A), and buffer solution. In the competitive assay, both the target analyte (A) and the reporter particles (P) can bind to the beads (B) to form the complexes BA and BP.

$$B + P \underset{k_d^1}{\overset{k_a^1}{\Leftrightarrow}} BP \text{ and } B + A \underset{k_d^2}{\overset{k_a^2}{\Leftrightarrow}} BA\ . \tag{44}$$

The target analyte cannot, however, bind to the reporter particles (P). We have four particle species, B, P, BP, and BA, in solution, and two fluid species (target analyte A and the buffer solution). Therefore, N_s=4 and N=6. Since the buffer solution is a passive component which does not interact biologically with the other species, one only needs to determine the volume fractions of the four particle species and the mass fraction of the target analyte A.

For convenience, we use the notation c_1=[B], c_2=[P], c_3=[BP], c_4=[BA], and c_5=[A]. In accordance with the reactions described in (44), the rate of production of each species is:

$$c_1' = -k_a^1 c_1 c_2 + k_d^1 c_3 - k_a^2 c_1 c_5 + k_d^2 c_4, \tag{45}$$

$$c_2' = -c_3' = -k_a^1 c_1 c_2 + k_d^1 c_3, \tag{46}$$

and

$$c_4' = -c_5' = k_a^2 c_1 c_5 - k_d^2 c_4. \tag{47}$$

Utilizing (19) and (45)-(47), we deduce the various mass transfer terms occurring in the competitive sedimentation biodetector.

5. Sandwich Assay Sedimentation Biodetector

In the sandwich assay, the protein-conjugated reporter particles cannot bind directly to the protein-conjugated beads. The target analyte (A) can bind to the beads (B) to form the complex BA and then to the reporter particles (P) to form the complex BAP. Alternatively, the target analyte can bind to a reporter particle to form the complex AP and then to the bead B to form the sandwich BAP. Accordingly, the following reactions occur in the sandwich assay:

$$B + A \underset{k_d^1}{\overset{k_a^1}{\Leftrightarrow}} BA, \quad P + A \underset{k_d^2}{\overset{k_a^2}{\Leftrightarrow}} AP, \quad B + AP \underset{k_d^3}{\overset{k_a^3}{\Leftrightarrow}} BAP, \quad \text{and} \quad BA + P \underset{k_d^4}{\overset{k_a^4}{\Leftrightarrow}} BAP \tag{48}$$

Witness that we have five particle species, B, P, AP, BA and BAP, and two fluid species (the target analyte A and the buffer solution). Accordingly, N_s=5, and N=7. As in the competitive assay, the buffer solution is a passive fluid component, which does not react with any of the other species.

Let c_1=[B], c_2=[P], c_3=[AP], c_4=[BA], c_5=[BAP] and c_6=[A]. The reactions (48) imply the following rates of production of each species:

$$c_1' = -k_a^1 c_1 c_6 + k_d^1 c_4 - k_a^3 c_1 c_3 + k_d^3 c_5, \tag{49}$$

$$c_2' = -k_a^2 c_2 c_6 + k_d^2 c_3 - k_a^4 c_2 c_4 + k_d^4 c_5, \tag{50}$$

$$c_3' = k_a^2 c_2 c_6 - k_d^2 c_3 - k_a^3 c_1 c_3 + k_d^3 c_5, \tag{51}$$

$$c_4' = k_a^1 c_1 c_6 - k_d^1 c_4 - k_a^4 c_2 c_4 + k_d^4 c_5, \tag{52}$$

$$c_5' = k_a^3 c_1 c_3 - k_d^3 c_5 + k_a^4 c_2 c_4 - k_d^4 c_5, \tag{53}$$

and

$$c_6' = -k_a^1 c_1 c_6 + k_d^1 c_4 - k_a^2 c_2 c_6 + k_d^2 c_3. \tag{54}$$

These reactions give rise to the mass transfer terms in the conservation equations.

6. **Results and Discussion**

In this section, we describe a sample of computations pertaining to both the competitive and sandwich assay formats. Based on previous works dealing with non-reacting species (Xue and Sun, 2003; Bürger et al., 2000c, 2001), we select n=4.65 and ϕ_{max}=0.6. The interstitial void fraction of closely packed spherical beads is approximately 0.4 and the solid fraction is 0.6. We consider a reactor of height L=10cm and a buffer solution of viscosity $\mu_f = 10^{-3}$Pa·s. In all the simulations, J=400, and λ=1s/m. Numerical tests indicate that further refinements of grid spacing do not lead to significant changes in the computational results. The properties of the various species, the target analyte, and the buffer solution are summarized in Table 1.

The beads (B) and the reporter particles (P) are considered to be spheres. The complexes are approximated as spherical particles with a volume that is equivalent to the total volume of their components. For example, the effective diameter of the complex BP is $d_{BP} = (d_B^3 + d_P^3)^{1/3} \approx d_B$. Likewise, $\rho_{BP} = \left(\rho_B d_B^3 + \rho_P d_P^3\right) / d_{BP}^3 \approx \rho_B$ is the apparent density of the complex BP.

The reactor is filled with a well-mixed suspension of reporter particles P, beads B, and target analyte A with the initial concentrations [B]=[B]$_0$, [P]= [P]$_0$, and [A]=[A]$_0$. One can

consider two extreme cases. In the first extreme, there are no formed complexes at the start of the settling process. In the case of the competitive assay, $[BP]_0 = [BA]_0 = 0$. In the case of the sandwich assay, $[BA]_0 = [AP]_0 = [BAP]_0 = 0$. In the other extreme, there is a thermodynamic equilibrium between the species and their complexes. In the interest of space, we will report here only results for the former case, which can be considered the worst case scenario. The rate constants of the various interactions are listed in Table 2.

6.1 Competitive Sedimentation Biodetector

We first describe the process in the absence of target analytes. See Fig. 2a for a schematic depiction. The simulation starts with a well mixed, un-reacted suspension of beads, reporter particles, and target analytes at concentrations $[B]_0 = 10$ nM, $[P]_0 = 1$ nM and $[A]_0 = 0$. As time goes by, the reporter particles interact with the beads to form the complex BP. Since the beads and the bead-reporter particle complexes are relatively heavy, they settle, leaving behind in the bulk of the solution a low concentration of reporter particles. The concentrations of the complex BP and the reporter particles P as functions of space and time are depicted, respectively, in Figs. 3 and 4. Since the reporter particles are very small, they tend to stay in solution for a very long period of time. Most of the sediment consists of beads and bead-reporter particle complexes. Since the initial concentration of the beads is relatively small, the sediment layer is very thin. At the conclusion of the bead's sedimentation process, there are just a few reporter particles left in the bulk of the solution. The lack of reporter particles in the bulk of the solution and their presence in the sediment indicates the absence of the target analyte. Witness the excess of reporter particles at the surface of the reaction chamber (Fig. 4, x=0.1 m). This accumulation is known as the Smith effect (Smith, 1966). Briefly, as the larger particles B and BP settle, they induce an upward fluid motion that propels the smaller particles (P) towards the top surface of the reactor.

The situation is quite different when the target analytes are present. In this case, the

target analytes compete with the reporter particles for binding sites on the beads. The process is depicted schematically in Fig. 2b. Fig. 5 depicts the concentration of the reporter particles (P) as a function of space and time when the initial concentration of the target analyte is $[A]_0$=10 nM.. Fig. 5 should be contrasted with Fig. 4. In the presence of the target analytes, fewer reporter particles bind to the beads and a larger number of reporter particles remains in suspension. As the target analyte concentration increases, the concentration of the complex BP decreases and the concentration of free reporter particles increases. An increase in the reporter particles' concentration in suspension indicates a higher target analyte concentration.

For clarity, the results of Figs. 3-5 are depicted again in Fig. 6 in a slightly different way. The detected signal (S) is proportional to the combined concentrations of the free reporter particles and the bead-bound reporter particles, S=[P]+[BP]. Fig. 6 depicts the S as a function of *x* at times t=10 min (a), t=20 min (b), and t=30 min (c). The figure mimics the signal that would be read by a scanner. The solid and dashed lines correspond to the cases of the presence and absence of the target analytes. For better visibility, the figures are truncated at S~1.1 nM. Much higher levels of S are observed in the sediment layer. Clearly, the signal in the buffer solution is much higher in the presence of the target analyte (solid line) than in its absence (dashed line). At t=30 min, the signal is nearly fully developed and changes very slowly as time increases (t>30 min).

6.2 Sandwich Sedimentation Biodetector

In the absence of the target analyte A (i.e., $[A]_0$=0), the protein-conjugated reporter particles P cannot bind to the protein-conjugated beads B, and there are only two particle species B and P in solution. Since the beads B settle much faster than the reporter particles P, eventually the beads B accumulate at the reactor's bottom, leaving the reporter particles in suspension. The presence of a high concentration of reporter particles in suspension indicates the absence of the target analyte. The process is depicted schematically in Fig. 1a.

Fig. 7 depicts quantitatively the concentration of the reporter particles P as a function of time and space. Witness that the concentration of the reporter particles is nearly uniform throughout most of the reactor chamber; but it declines sharply next to the bottom, in the region occupied by the settling beads. To better visualize the concentration distribution of the reporter particles P next to the bottom, Fig. 8 depicts the concentration of reporter particles P as a function of time at various x-locations. When the heavier beads B settle, they displace the lighter particles P, leading to a lower concentration of the indicator particles P in the sediment layer. Witness the oscillations in the reporter particle concentration in the lower part of the reactor. These oscillations are caused by the interactions between the downward wave associated with the settling of the beads and the upward wave associated with the movement of the liquid and reporter particles. Eventually these oscillations decay.

Next, we investigate the effect of the target analyte concentration on the bead and reporter particles' distributions. When the target analytes are present, the reporter particles can bind to the beads and settle. Thus, the presence of target analyte is indicated by the depletion of reporter particles in the supernatant. The process is depicted schematically in Fig. 1b.

Figs. 9 and 10 depict, respectively, the concentrations of the complex AP and the free reporter particles P as functions of space and time when the initial target analyte concentration $[A]_0$=10 nM. The rate of formation of the complex AP is highest at time t=0, and it decreases as time increases. As in Fig. 4, the Smith effect (Smith, 1966) which causes an excess concentration of reporter particles next to the surface of the reaction chamber (x=0.1 m), is evident in both Figs. 9 and 10. Due to the binding of AP with the beads B to form the complex BAP, Fig. 9 depicts a low concentration of the AP complexes throughout most of the chamber's volume. In the presence of target analyte, there are few free reporter particles (Fig.10) in the bulk of the solution.

The measured signal is proportional to the total concentration of the reporter particles S=[P]+[AP]+[BAP]. Fig. 11 depicts the signal level S in the presence of the target analyte at

initial concentration $[A]_0$=10 nM (solid lines) and in the absence of the target analyte (dashed lines) at times 10 minutes (a), 20 minutes (b), and 30 minutes (c). For better visibility, the figure is truncated at S~1.1 nM. Fig. 11 mimics the signal that would have been detected with a scanner. Only very slow changes are observed after 30 minutes, indicating that the signal is nearly fully developed within the first 30 minutes. In the absence of the target analyte (dashed lines), the supernatant's signal is much higher than in the presence of the target analyte (solid line).

7. **Conclusions**

A mathematical model and numerical scheme for modeling sedimentation bioreactors is proposed. The model allows one to predict the spatial and temporal distributions of each species' concentration under various conditions. Our model is a fusion of two previously well-studied models: a mathematical model for the sedimentation of particles of various sizes in the absence of biological interactions and a model for biological interactions in the presence of a specified flow field. The predictions of the sedimentation model for the settling of poly-disperse suspensions with particles of various sizes and densities in the absence of biological interactions were compared and favorably agreed with the experimental observations of Smith (1965), Selim et al. (1983), El-Genk et al. (1985), Law et al. (1987), Xue and Sun (2003), and Xue et al. (2003). The predictions of the biological interactions model that accounts for mass transfer when the flow field is apriori known were also compared and favorably agreed with experimental data (Qian and Bau, 2003 and 2004). We were not able to find in the existing literature any experimental data for the sedimentation reactor that we studied here. Nevertheless, the agreement between the model's predictions and experimental data in the special cases discussed above gives us confidence that the theoretical predictions are reliable.

We hope that the model presented here will be useful to designers of sedimentation biodetectors. The simulations can be used to predict reactor performance as well as to assist in the selection of reporter particle and bead concentrations to achieve optimal detection conditions

for a specified concentration range of target analytes. Although the numerical simulations cannot substitute for experiments, they can help narrow the experimental parameter space, shorten the development process, and increase the probability of success.

The presence of target analytes both in the competitive and sandwich assays is detected by monitoring the concentration of reporter particles in the bulk of the solution. In the case of the sandwich assay, depletion in the reporter particle concentration indicates the presence of target analyte. In contrast, in the case of the competitive assay, the presence of reporter particles in the bulk of the solution indicates the presence of target analyte.

The computations indicate the sedimentation process is relatively slow. The sedimentation of the beads can be significantly accelerated by selecting larger diameter beads and/or by using centrifugal, magnetic, and electric fields to increase the settling force. Of course, the sedimentation time must be long enough to allow sufficient time for the biological interactions.

The work presented here can be expanded in a number of directions. Better models are needed for the interactions between molecules in solution and particles. The reactor can be modified to act as a flow-through reactor. In that case the unbound target analytes and reporter particles will be free to flow through a membrane while the beads and the bead-target analyte-reporter particle complexes will remain behind.

APPENDIX:

In this appendix, we provide additional details on the implementation of the numerical scheme. We first describe the procedures used to calculate the flux $\mathbf{h}_{j\pm1}^{n}$. Given the vector $\overline{\mathbf{W}}_{j}^{n}$ (j=1, 3,…, J-1), we construct a piecewise linear interpolation of W_j^n at time t_n. To this end, we need to determine the slope vector $\mathbf{W}'_j = (W'_{1,j},\ldots,W'_{N,j})^T$ (j=1, 3,…, J-1), where

$$W'_{i,j} = \begin{cases} 0 & \text{when} j=1 \text{ and } j=J-1 \\ MM\left\{\theta\left(\overline{W}_{i,j}^{n}-\overline{W}_{i,j-2}^{n}\right),\left(\overline{W}_{i,j+2}^{n}-\overline{W}_{i,j-2}^{n}\right)/2,\theta\left(\overline{W}_{i,j+2}^{n}-\overline{W}_{i,j}^{n}\right)\right\} & \text{when} j=3,5,\ldots,J-3 \end{cases}, \quad \text{(A1)}$$

i=1,…,N, and

$$MM(a,b,c) = \begin{cases} \min(a,b,c) & \text{when a, b, c} > 0 \\ \max(a,b,c) & \text{when a, b, c} < 0 \\ 0 & \text{otherwise} \end{cases} \quad \text{(A2)}$$

is the *minmod* function and $\theta \in (0,2)$. The choice of θ is problem-dependent (Berres et al., 2003). In our simulations, we used $\theta=1.3$.

The values of $\mathbf{W}$ and the maximal wave speeds at the cell boundaries x_j (j=2, 4, …, J-2) are, respectively,

$$\mathbf{W}_j^{\mp} = \overline{\mathbf{W}}_{j\mp1}^{n} \pm \frac{1}{2}\mathbf{W}'_{j\mp1}, \quad j=2,4,\ldots,J-2 \quad \text{(A3)}$$

and

$$a_j^n = \max\left\{\rho\left(\mathbf{J}_F(\mathbf{W}_j^-)\right),\rho\left(\mathbf{J}_F(\mathbf{W}_j^+)\right)\right\}, \quad j=2,4,\ldots,J-2, \quad \text{(A4)}$$

where $\mathbf{J}_F(\mathbf{W}) = \partial F_i(\mathbf{W},q)/\partial W_j$ (i, j=1,…,N) is the Jacobian of $\mathbf{F}(\mathbf{W},q)$; $\lambda_i(\mathbf{J}_F)$ is the i-th eigenvalue of the matrix $\mathbf{J_F}$; and $\rho(\mathbf{J}_F) = \max_i|\lambda_i(\mathbf{J}_F)|$ is the spectral radius of $\mathbf{J_F}$. Consistent with our order of magnitude analysis, $\partial q/\partial W_j$ is small compared to the other terms in the Jacobian, and we set $\partial q/\partial W_j \approx 0$.

The half-cell averages of the left ($[x_{j-1}, x_j]$) and the right ($[x_j, x_{j+1}]$) half-cells adjacent to $x=x_j$ are denoted, respectively, with subscripts L and R.

$$\mathbf{W}_{j,L}^{n} = \overline{\mathbf{W}}_{j-1}^{n} + \left(\frac{1}{2} - \lambda a_j^n\right)\mathbf{W}'_{j-1}, \quad j = 2,4,..., J-2 \tag{A5}$$

and

$$\mathbf{W}_{j,R}^{n} = \overline{\mathbf{W}}_{j+1}^{n} - \left(\frac{1}{2} - \lambda a_j^n\right)\mathbf{W}'_{j+1}, \qquad j = 2,4,..., J-2. \tag{A6}$$

The flux slope vector

$$\mathbf{F}'(\mathbf{W}_{j,c}^{n}) = \left(F_1'(\mathbf{W}_{j,c}^{n}),\ldots, F_N'(\mathbf{W}_{j,c}^{n})\right)^T, \quad c = L, R \text{ and } j = 3,4,..., J-3 \tag{A7}$$

$$F_i'(\mathbf{W}_{2,c}^{n}) = F_i'(\mathbf{W}_{J-2,c}^{n}) = 0, \quad c = L, R \tag{A8}$$

and

$$F_i'(\mathbf{W}_{j,c}^{n}) = MM\{\alpha, \beta, \vartheta\}, \quad c = L, R;\ i = 1,...,N;\ \text{and } j = 4,6,...,J-4. \tag{A9}$$

In the above,

$$\alpha = \theta\left(F_i(\mathbf{W}_{j,c}^{n}, \tilde{q}^{n}(x_j)) - F_i(\mathbf{W}_{j-2,c}^{n}, \tilde{q}^{n}(x_{j-2}))\right), \tag{A10}$$

$$\beta = \left(F_i(\mathbf{W}_{j+2,c}^{n}, \tilde{q}^{n}(x_{j+2})) - F_i(\mathbf{W}_{j-2,c}^{n}, \tilde{q}^{n}(x_{j-2}))\right)/2, \tag{A11}$$

$$\vartheta = \theta\left(F_i(\mathbf{W}_{j+2,c}^{n}, \tilde{q}^{n}(x_{j+2})) - F_i(\mathbf{W}_{j,c}^{n}, \tilde{q}^{n}(x_j))\right), \tag{A12}$$

The function $\tilde{q}^{n}(x)$ is the approximation of the function $q(x, t_n)$ obtained from the solution vector $\overline{\mathbf{W}}_j^n$ by a quadrature rule applied to (37). For example,

$$\tilde{q}^{n}(x) = 2\Delta x \sum_{j=1}^{l} \tilde{m}\left(\overline{\mathbf{W}}_{2j-1}^{n}\right) + (x - x_{2l})\tilde{m}\left(\overline{\mathbf{W}}_{2l+1}^{n}\right) \text{ when } x \in (x_{2l}, x_{2l+2}] \tag{A13}$$

We calculate the midpoint values with Taylor series expansions:

$$\mathbf{W}_{j,c}^{n+1/2} = \mathbf{W}_{j,c}^{n} - \frac{\lambda}{2}\mathbf{F}'(\mathbf{W}_{j,c}^{n}), \text{ c} = L, R \text{ and } j = 2,4,..., J-2. \tag{A14}$$

Next, we define the cell averages at time t=(n+1)Δt:

$$\overline{\boldsymbol{\psi}}_j^{n+1} = \frac{\left(\overline{\mathbf{W}}_{j-1}^n + \overline{\mathbf{W}}_{j+1}^n\right)}{2} + \frac{\left(1-\lambda a_j^n\right)\left(\mathbf{W}'_{j-1} - \mathbf{W}'_{j+1}\right)}{4} - \frac{1}{2a_j^n}\left[\mathbf{F}\left(\mathbf{W}_{j,R}^{n+1/2}, \tilde{q}^{n+1/2}\left(x_j + \frac{a_j^n \Delta t}{2}\right)\right) - \mathbf{F}\left(\mathbf{W}_{j,L}^{n+1/2}, \tilde{q}^{n+1/2}\left(x_j - \frac{a_j^n \Delta t}{2}\right)\right)\right], \quad j = 2,4,...,J-2 \tag{A15}$$

over the non-uniform interval $[x_j - a_j^n \Delta t, x_j + a_j^n \Delta t]$ and

$$\overline{\boldsymbol{\psi}}_j^{n+1} = \overline{\mathbf{W}}_j^n - \frac{\lambda\left(a_{j+1}^n - a_{j-1}^n\right)\mathbf{W}'_j}{2} - \frac{\lambda}{1-\lambda\left(a_{j-1}^n + a_{j+1}^n\right)}\left[\mathbf{F}\left(\mathbf{W}_{j+1,L}^{n+1/2}, \tilde{q}^{n+1/2}\left(x_j - \frac{\Delta x - a_{j-1}^n \Delta t}{2}\right)\right) - \mathbf{F}\left(\mathbf{W}_{j-1,R}^{n+1/2}, \tilde{q}^{n+1/2}\left(x_j + \frac{\Delta x - a_{j+1}^n \Delta t}{2}\right)\right)\right], \quad j = 3,5,..., J-3 \tag{A16}$$

over the interval $[x_{j-1} + a_{j-1}^n \Delta t, x_{j+1} - a_{j+1}^n \Delta t]$. In the above,

$$\tilde{q}^{n+1/2}(x) = \Delta x \sum_{j=1}^{l}\left[\tilde{m}\left(\mathbf{W}_{2j-1,L}^{n+1/2}\right) + \tilde{m}\left(\mathbf{W}_{2j-1,R}^{n+1/2}\right)\right] + \begin{cases} (x - x_{2l})\tilde{m}\left(\mathbf{W}_{2l+1,L}^{n+1/2}\right) & \text{when } x \in [x_{2l}, x_{2l+1}), \\ \Delta x \tilde{m}\left(\mathbf{W}_{2l+1,L}^{n+1/2}\right) + (x - x_{2l+1})\tilde{m}\left(\mathbf{W}_{2l+1,R}^{n+1/2}\right) & \text{when } x \in [x_{2l+1}, x_{2l+2}). \end{cases} \tag{A17}$$

Using both families of the approximate cell averages, we determine the vector of discrete derivatives: $\boldsymbol{\psi}'_j = (\psi'_{1,j}, \ldots, \psi'_{N,j})^T \left(j = 2,4,..., J-2\right)$, where $\boldsymbol{\psi}'_2 = \boldsymbol{\psi}'_{J-2} = 0$ and

$$\psi'_{i,j} = \frac{1}{\Delta x} MM\left\{\theta \frac{\overline{\psi}_{i,j}^{n+1} - \overline{\psi}_{i,j-1}^{n+1}}{1+\lambda\left(a_j^n - a_{j-2}^n\right)}, \frac{\overline{\psi}_{i,j+1}^{n+1} - \overline{\psi}_{i,j-1}^{n+1}}{2+\lambda\left(2a_j^n - a_{j-2}^n - a_{j+2}^n\right)}, \theta \frac{\overline{\psi}_{i,j+1}^{n+1} - \overline{\psi}_{i,j}^{n+1}}{1+\lambda\left(a_j^n - a_{j+2}^n\right)}\right\} \tag{A18}$$

for (i=1,…,N) and (j=4,6,…, J–4).

Next, we calculate the desired numerical flux vectors:

$$\mathbf{h}_j^n = \frac{1}{2}\left[\mathbf{F}\left(\mathbf{W}_{j,R}^{n+1/2}, \tilde{q}^{n+1/2}\left(x_j + \frac{\Delta x}{2}\right)\right) + \mathbf{F}\left(\mathbf{W}_{j,L}^{n+1/2}, \tilde{q}^{n+1/2}\left(x_j - \frac{\Delta x}{2}\right)\right)\right] - \frac{a_j^n\left(\overline{\mathbf{W}}_{j+1}^n - \overline{\mathbf{W}}_{j-1}^n\right)}{2} + \frac{a_j^n(1-\lambda a_j^n)\left(\mathbf{W}'_{j-1} + \mathbf{W}'_{j+1}\right)}{4} + \lambda \Delta x\left(a_j^n\right)^2 \boldsymbol{\psi}'_j, \quad j = 2,4,..., J-2 \tag{A19}$$

Finally, we outline the procedure to calculate the source term. An overview of various discretization schemes of source terms such as **S**(**W**) appearing in (32) is given in Russo (2002). In our application, the source terms are not stiff, and we utilize a fully explicit time

discretization. To this end, we replace the formula for calculating the predictor solution values at $t=t_{n+1/2}$, (A14), with

$$\mathbf{W}_{j,c}^{n+1/2} = \mathbf{W}_{j,c}^{n} - \frac{\lambda}{2}\mathbf{F}'\left(\mathbf{W}_{j,c}^{n}\right) + \frac{\Delta t}{2}\mathbf{S}\left(\mathbf{W}_{j,c}^{n}\right), \quad c = L, R, \quad j = 2,4,...,J-2, \tag{A20}$$

$$\mathbf{S}_{j}^{n} = \frac{1}{2}\left[\mathbf{S}\left(\mathbf{W}_{j+1,L}^{n+1/2}\right) + \mathbf{S}\left(\mathbf{W}_{j-1,R}^{n+1/2}\right)\right], \quad j = 3,5,...,J-3, \tag{A21}$$

$$\mathbf{S}_{1}^{n} = \mathbf{S}\left(\overline{\mathbf{W}}_{1}^{n}\right), \tag{A22}$$

and

$$\mathbf{S}_{J-1}^{n} = \mathbf{S}\left(\overline{\mathbf{W}}_{J-1}^{n}\right). \tag{A23}$$

Acknowledgments

The work described in this paper was supported, in part, by the NIH Grant 1U01 DE 14964-01 and by the DARPA SIMBIOSYS Program (N66001-01-C-8056). We also acknowledge support by the Collaborative Research Center (Sonderforschungsbereich) 404 at the University of Stuttgart.

References

1. Arastoopour, H., Lin, S.C., Weil, S.A., 1982. Analysis of vertical pneumatic conveying of solids using multiphase flow models. AICHE J., 28, 467–473.
2. Batchelor, G.K., 1982. Sedimentation in a dilute polydisperse system of interacting spheres. Part 1. General theory. J. Fluid Mech., 119, 379–408.
3. Batchelor, G.K., Wen, C.S., 1982. Sedimentation in a dilute polydisperse system of interacting spheres. Part 2. Numerical results. J. Fluid Mech., 124, 495–528.
4. Berres, S., Bürger, R., Karlsen K.H., Tory, E.M., 2003. Strongly degenerate parabolic-hyperbolic systems modeling polydisperse sedimentation with compression. SIAM J. Appl. Math., 64, 41–80.
5. Berres, S., Bürger, R., Karlsen, K.H., 2004a. Central schemes and systems of conservation laws with discontinuous coefficients modeling gravity separation of polydisperse suspensions. J. Comp. Appl. Math., 164-165, 53–80.
6. Berres, S., Bürger, R., Tory, E.M., 2004b. Applications of polydisperse sedimentation models. Chem. Eng. J., to appear.
7. Berres, S., Bürger, R., Tory, E.M., 2005. On mathematical models and numerical simulation of the fluidization of polydisperse suspensions. Applied Mathematical Modeling, 29, 159193.

8. Bürger, R., Tory, E.M., 2000. On upper rarefaction waves in batch settling. Powder Technology, 108, 74–87.

9. Bürger, R., Wendland, W.L., Concha, F., 2000a. Model equations for gravitational sedimentation-consolidation processes. Z. Angew. Math. Mech. 80, 79–92.

10. Bürger, R., Concha, F., Tiller, F.M., 2000b. Applications of the phenomenological theory to several published experimental cases of sedimentation processes. Chem. Eng. J. 80, 105-117.

11. Bürger, R., Concha, F., Fjelde, K.K., Karlsen, K.H., 2000c. Numerical simulation of the settling of polydisperse suspensions of spheres. Powder Technology, 113, 30–54.

12. Bürger, R., Wendland, W.L., 2001. Sedimentation and suspension flows: Historical perspective and some recent developments. J. Eng. Math., 41, 101–116.

13. Bürger, R., Fjelde, K.K., Höfler, K., Karlsen, K.H., 2001. Central difference solutions of the kinematic model of settling of polydisperse suspensions and three-dimensional particle-scale simulations. J. Eng. Math., 41, 167–187.

14. Bürger, R., Karlsen, K.H., Tory, E.M., Wendland, W.L., 2002. Model equations and instability regions for the sedimentation of polydisperse suspensions of spheres. Z. Angew. Math. Mech., 82, 699–722.

15. Concha, F., Bürger, R., 2002. A century of research in sedimentation and thickening. KONA Powder and Particle, 20, 38–70.

16. Davis, R.H., Gecol, H., 1994. Hindered settling function with no empirical parameters for polydisperse suspensions. AICHE J., 40, 570–575.

17. Drew, D.A., Passman, S.L., 1999. Theory of multicomponent fluids, Springer-Verlag, New York, Inc.

18. El-Genk, M.S., Kim, S.-H., and Erickson, D., 1985. Sedimentation of binary mixtures of particles of unequal densities and of different sizes. Chemical Engineering Communications, 36, 99-119.

19. Feleszko, W., Maksymiuk, J., Oracz, G., Golicka, D., Szajewska, H., 2004. The TUBEX (TM) typhoid test detects current Salmonella infections. Journal of Immunological Methods, 285, 137–138.

20. House, D., Wain, J., Ho, V.A., Diep, T.S., Chinh, N.T., Bay, P.V., Vinh, H., Duc, M., Parry, C.M., Dougan, G., White, N.J., Hien, T.T., Farrar, J.J., 2001. Serology of typhoid fever in an area of endemicity and its relevance to diagnosis. Journal of Clinical Microbiology, 39, 1002–1007.

21. Kurganov, A., Tadmor, E., 2000. New high resolution central schemes for nonlinear conservation laws and convection-diffusion equations. Journal of Computational Physics, 160, 241–282.

22. Law, H.S., Masliyah, J.H., MacTaggart, R.S., Nandakumar, K., 1987. Gravity separation of bidisperse suspensions: light and heavy particle species, Chemical Engineering Science, 42, 1527–1538.

23. Lim, P.L., 1990. A one-step 2-particle latex immunoassay for the detection of salmonella-typhi endotoxin. Journal of Immunological Methods, 135, 257–261.

24. Lim, P.L., Ko, K.H., 1990. A tube latex test based on color separation for the detection of IgM antibodies to either one of 2 different microorganisms. Journal of Immunological Methods, 135, 9–14

25. Lim, P.L., Tam, F.C.H., Cheong, W.M., Jegathesan, M., 1998. One-step 2-minute test to detect typhoid-specific antibodies based on particle separation in tubes. Journal of Clinical Microbiology, 36, 2271–2278.

26. Lockett, M.J., Al-Habbooby, H.M., 1973. Differential settling by size of two particle species in a liquid. Transactions of the Institution of Chemical Engineers, 51, 281–292.

27. Lockett, M.J., Bassoon, K.S., 1979. Sedimentation of binary particle mixtures. Power Technol., 24, 1–7.

28. Masliyah, J.H., 1979. Hindered settling in a multi-species particle system. Chem. Eng. Sci., 34, 1166–1168.

29. Mirza, S., Richardson, J.F., 1979. Sedimentation of suspensions of particles of two or more sizes. Chem. Eng. Sci., 34, 447–454.

30. Nakamura, K., Capes, C.E., 1976. Vertical pneumatic conveying of binary particle mixtures. In: Fluidization Technology, Vol. 2, Keairns, D.L. (Eds.), Hemisphere Publishing, Washington, DC, 159–184.

31. Oracz, G., Feleszko, W., Golicka, D., Maksymiuk, J., Klonowska, A., Szajewska, H., 2003. Rapid diagnosis of acute Salmonella gastrointestinal infection. Clinical Infectious Diseases, 36, 112–115.

32. Qian, S., Bau, H.H., 2003. A mathematical model of lateral flow bio-reactions applied to sandwich assays. Analytical Biochemistry, 322, 89–98.

33. Qian, S., Bau, H.H., 2004. Analysis of lateral flow bio-detector: competitive assay. Analytical Biochemistry, 326, 211–224.

34. Richardson, J. F., Zaki, W.N., 1954. Sedimentation and fluidization: Part I. Trans. Inst. Chem. Engrs. (London), 32, 35–53.

35. Russo, G., 2002. Central Schemes and Systems of Balance Laws, In: Meister, A., and Struckmeier, J., (Eds.), Hyperbolic Partial Differential Equations, Theory, Numerics and Applications, Vieweg, Braunschweig, 59–114.

36. Schuck, P., 1998. Sedimentation analysis of noninteracting and self-associating solutes using numerical solutions to the Lamm equation. Biophysical Journal, 75, 1503–1521.

37. Schuck, P., 2004a. A model for sedimentation in inhomogeneous media. I. Dynamic density gradients from sedimenting co-solutes. Biophysical Chemistry, 108, 187–200.

38. Schuck, P., 2004b. A model for sedimentation in inhomogeneous media. II. Compressibility of aqueous and organic solvents. Biophysical Chemistry, 108, 201–214.

39. Selim, M.S., Kothari, A.C., Turian, R.M., 1983. Sedimentation of multisized particles in concentrated suspensions. AICHE J., 29, 1029–1038.

40. Sharma, R.V., Edwards, R.T., Beckett, R., 1993. Physical characterization and quantification of bacteria by sedimentation field-flow fractionation. Appl. Environ. Microbiol., 59, 1864–1875.

41. Shih, Y.T., Gidaspow, D., Wasan, D.T., 1987. Hydrodynamics of sedimentation of multisized particles, Powder Technology, 50(1987), 201–215

42. Smith, T.N., 1965. The differential sedimentation of particles of two different species. Transactions of the Institution of Chemical Engineers, 43, T69–T73.

43. Smith, T.N., 1966. The sedimentation of particles having a dispersion of sizes. Transactions of the Institution of Chemical Engineers, 44, 153–157.

44. Stafford, W.F., Braswell, E.H., 2004. Sedimentation velocity, multi-speed method for analyzing polydisperse solutions. Biophysical Chemistry, 108, 273–279.

45. Tam, F.C.H., Lim, P.L., 2003. The TUBEX (TM) typhoid test based on particle-inhibition immunoassay detects IgM but not IgG anti-O9 antibodies. Journal of Immunological Methods, 282, 83–91.

46. Tory, E.M., Ford, R.A., 2004. Simulation of sedimentation of bidisperse suspensions. Int. J. Mineral Process, 73, 119–130.

47. Xue, B., Sun, Y., 2003. Modeling of sedimentation of polydisperse spherical beads with a broad size distribution. Chem. Eng. Sci., 58, 1531–1543.

48. Xue, B., Tong, X., Sun, Y., 2003. Polydisperse model for the hydrodynamics of expanded bed adsorption systems. AIChE J., 49, 2510 – 2518.

49. Zeidan, A., Rohani, S., Bassi, A., 2004. Dynamic and steady-state sedimentation of polydisperse suspension and prediction of outlets particle-size distribution. Chemical Engineering Science, 59, 2619–2632.

List of Captions

1. A schematic diagram of the sedimentation biodetector operating in a sandwich assay format in the absence (A) and presence (B) of target analytes. I and II denote, respectively, initial and final conditions. The symbols ● , ○ , and ✸ represent, respectively, the bead (B), the indicator particle (P), and the target analyte (A).

2. A schematic diagram of the sedimentation bio-detector operating in a competitive assay format in the absence (A) and presence (B) of target analytes. I and II denote, respectively, initial and final conditions. The symbols ● , ○ , and ✸ represent, respectively, the bead (B), the indicator particle (P), and the target analyte (A).

3. The concentration of the complex BP in the competitive sedimentation biodetector as a function of space and time. $[A]_0$=0 nM, $[B]_0$=10 nM, and $[P]_0$=1 nM.

4. The concentration of the reporter particles P in the competitive sedimentation biodetector as a function of space and time. $[A]_0$=0, $[B]_0$=10 nM, and $[P]_0$=1 nM.

5. The concentration of the reporter particles P in the competitive sedimentation biodetector as a function of space and time. $[A]_0$=10 nM, $[B]_0$=10 nM, and $[P]_0$=1 nM.

6. The signal S=[P]+[BP] as a function of *x* at 10 minutes (a), 20 minutes (b), and 30 minutes (c) in the presence $[A]_0$=10 nM (solid line) and in the absence of target analyte $[A]_0$=0 (dashed line) during the competitive sedimentation biodetector.

7. The concentration of the reporter particles P in the sandwich sedimentation biodetector as a function of space and time. $[A]_0$=0, $[B]_0$=10 nM, and $[P]_0$=1 nM.

8. The concentration of the reporter particles P in the sandwich sedimentation biodetector as a function of time at various locations near the bottom of the reactor. $[A]_0$=0, $[B]_0$=10 nM, and

$[P]_0$=1 nM.

9. The concentration of the complex AP in the sandwich sedimentation biodetector as a function of space and time. $[A]_0$=10 nM, $[B]_0$=10 nM, and $[P]_0$=1 nM.

10. The concentration of the reporter particles P in the sandwich sedimentation biodetector as a function of space and time. $[A]_0$=10 nM, $[B]_0$=10 nM, and $[P]_0$=1 nM.

11. The signal S=[P]+[BP]+[BAP] as a function of *x* at 10 minutes (a), 20 minutes (b), and 30 minutes (c) in the presence of target analyte $[A]_0$=10 nM (solid line) and in the absence of target analyte $[A]_0$=0 nM (dashed line) during the sandwich sedimentation reactor.

LIST OF TABLES

1. The material properties of the particle and fluid species involved in the competitive and sandwich formats

2. The interaction rate constants of the reactions involved in the competitive and sandwich formats

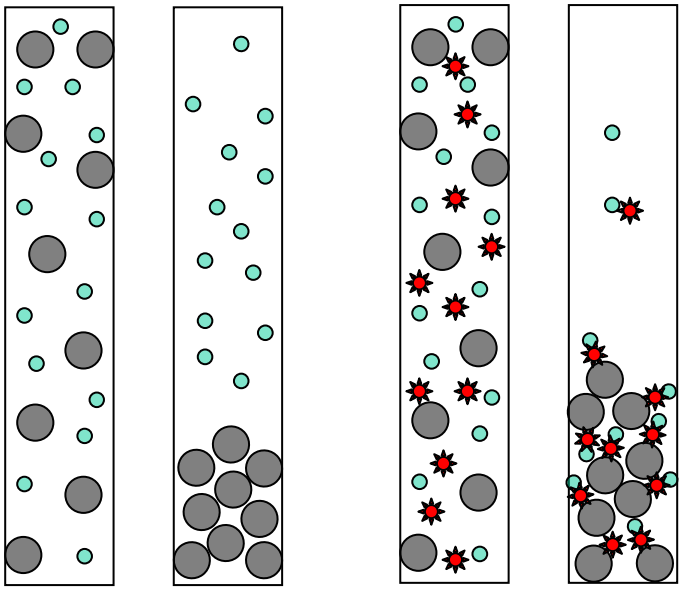

Fig.1: A schematic diagram of the sedimentation biodetector operating in a sandwich assay format in the absence (A) and presence (B) of target analytes. I and II denote, respectively, initial and final conditions. The symbols ● , ○ , and ✸ represent, respectively, the bead (B), the indicator particle (P), and the target analyte (A).

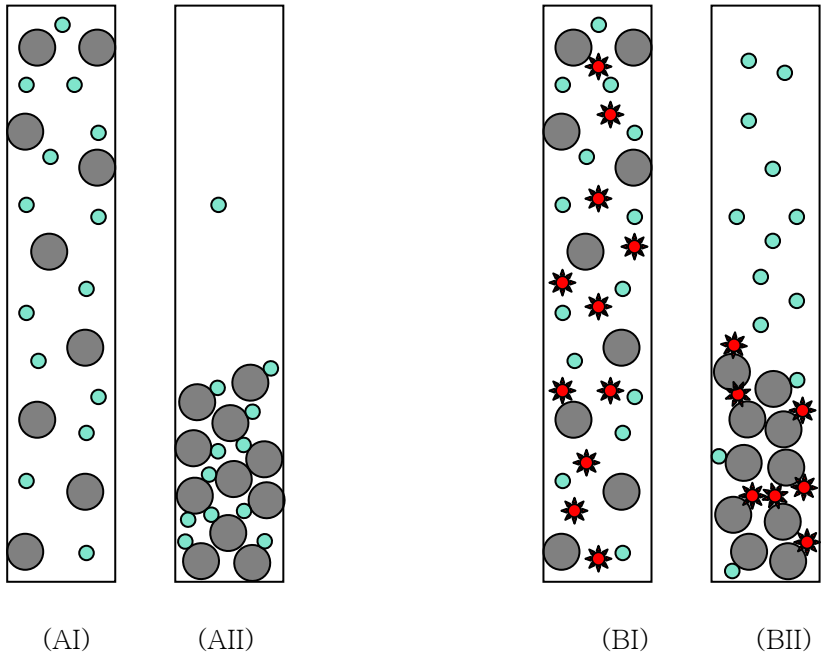

Fig.2: A schematic diagram of the sedimentation bio-detector operating in a competitive assay format in the absence (A) and presence (B) of target analytes. I and II denote, respectively, initial and final conditions. The symbols ● , ○ , and ✸ represent, respectively, the bead (B), the indicator particle (P), and the target analyte (A).

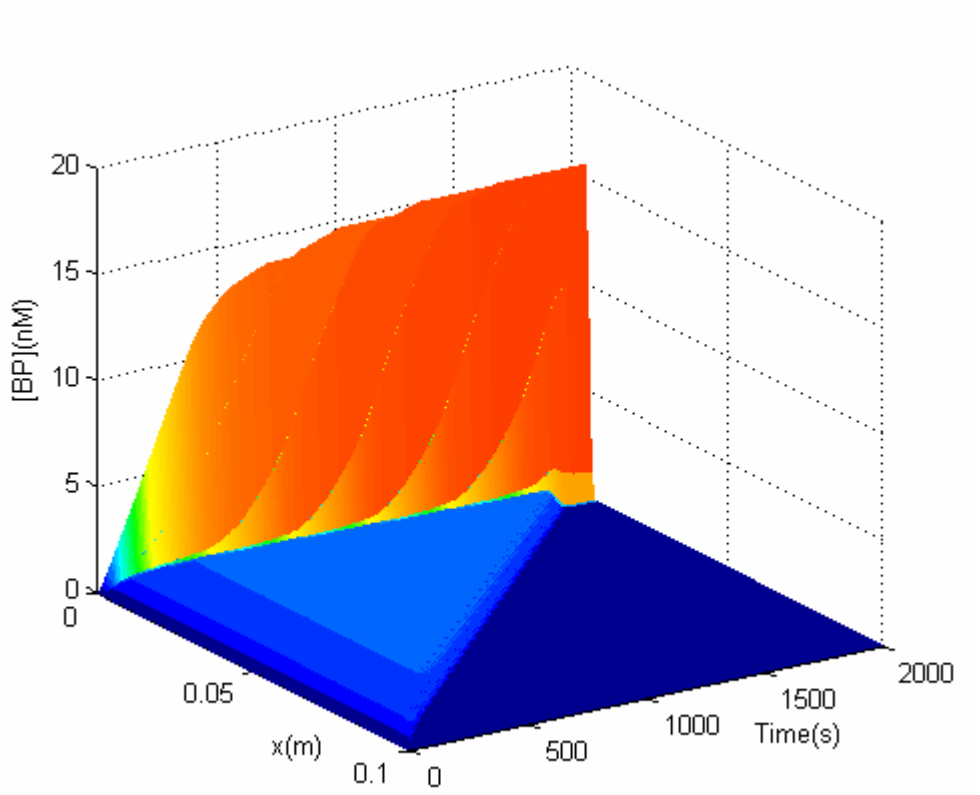

Fig.3: The concentration of the complex BP in the competitive sedimentation biodetector as a function of space and time. $[A]_0$=0 nM, $[B]_0$=10 nM, and $[P]_0$=1 nM.

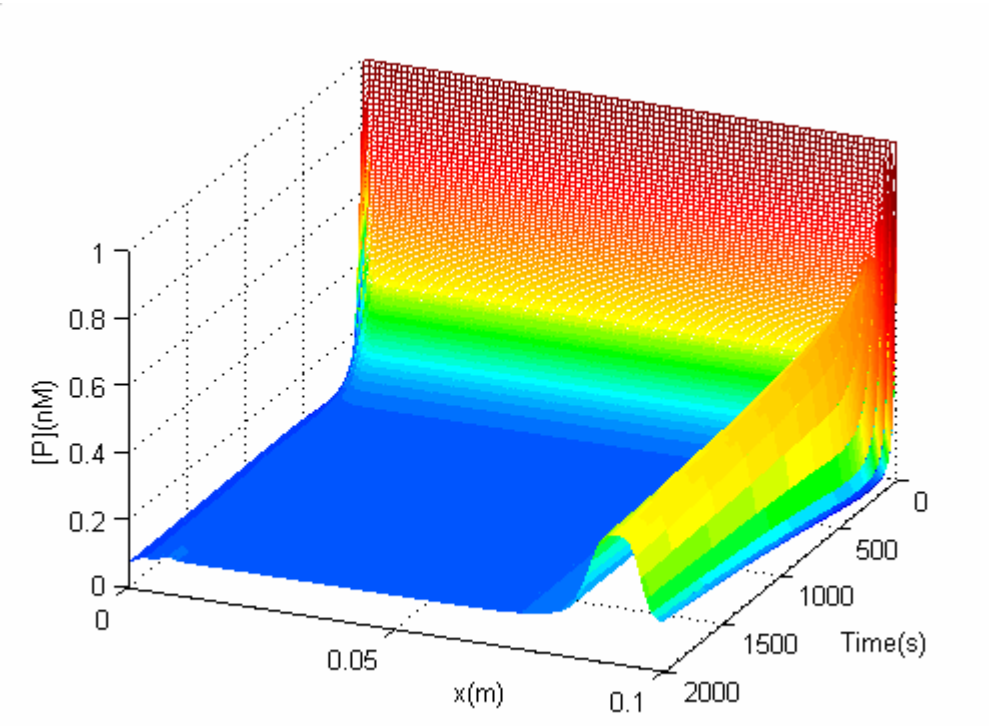

Fig.4: The concentration of the reporter particles P in the competitive sedimentation biodetector as a function of space and time. $[A]_0$=0, $[B]_0$=10 nM, and $[P]_0$=1 nM.

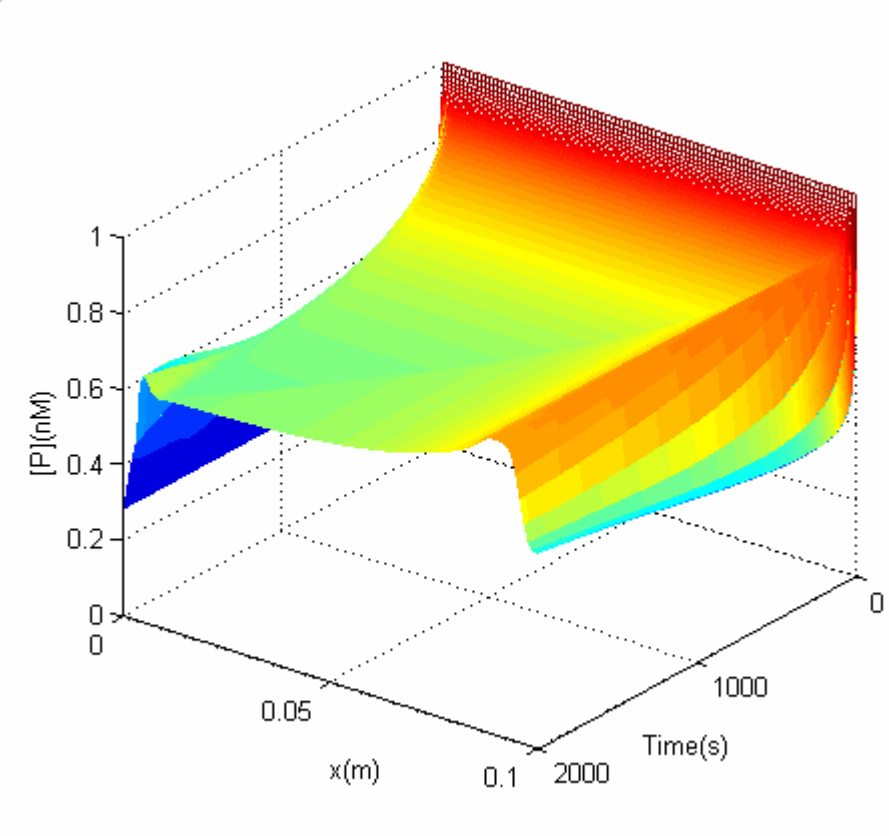

Fig.5: The concentration of the reporter particles P in the competitive sedimentation biodetector as a function of space and time. $[A]_0$=10 nM, $[B]_0$=10 nM, and $[P]_0$=1 nM.

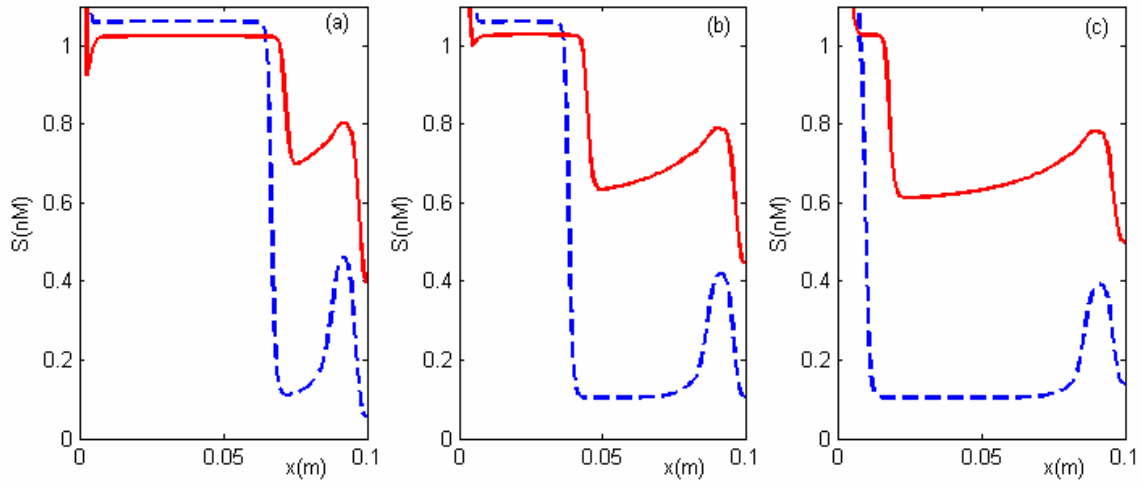

Fig.6: The signal S=[P]+[BP] as a function of *x* at 10 minutes (a), 20 minutes (b), and 30 minutes (c) in the presence $[A]_0$=10 nM (solid line) and in the absence of target analyte $[A]_0$=0 (dashed line) during the competitive sedimentation biodetector.

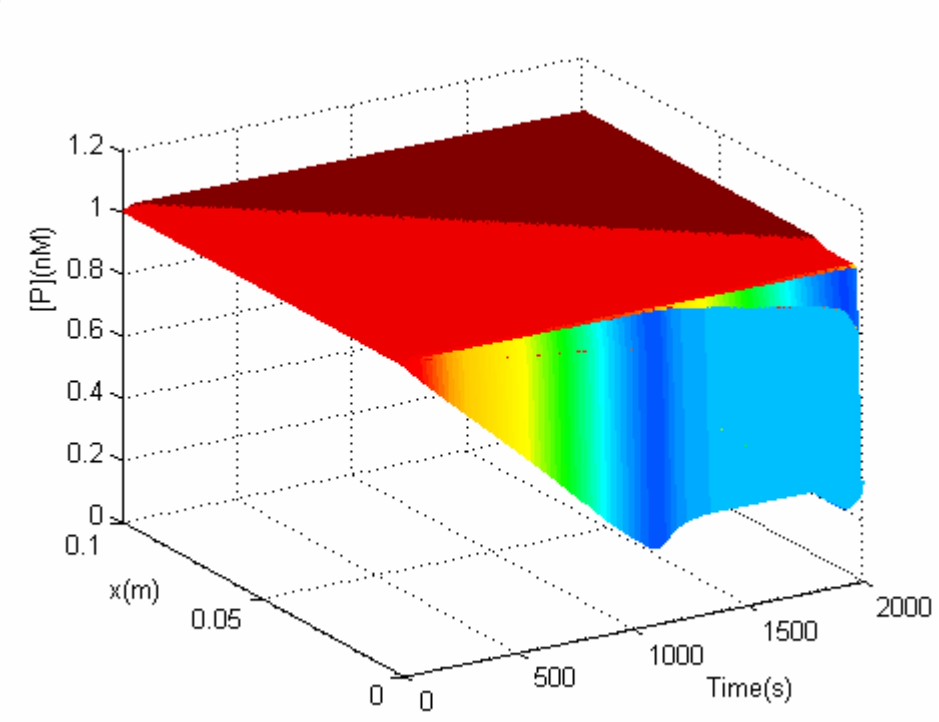

Fig.7: The concentration of the reporter particles P in the sandwich sedimentation biodetector as a function of space and time. $[A]_0$=0, $[B]_0$=10 nM, and $[P]_0$=1 nM.

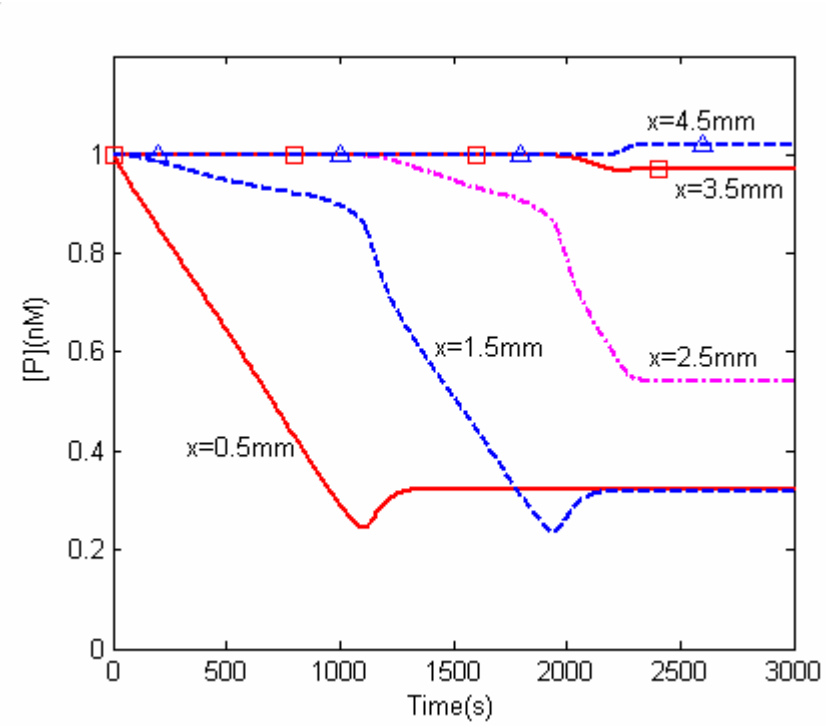

Fig.8: The concentration of the reporter particles P in the sandwich sedimentation biodetector as a function of time at various locations near the bottom of the reactor. $[A]_0=0$, $[B]_0=10$ nM, and $[P]_0=1$ nM.

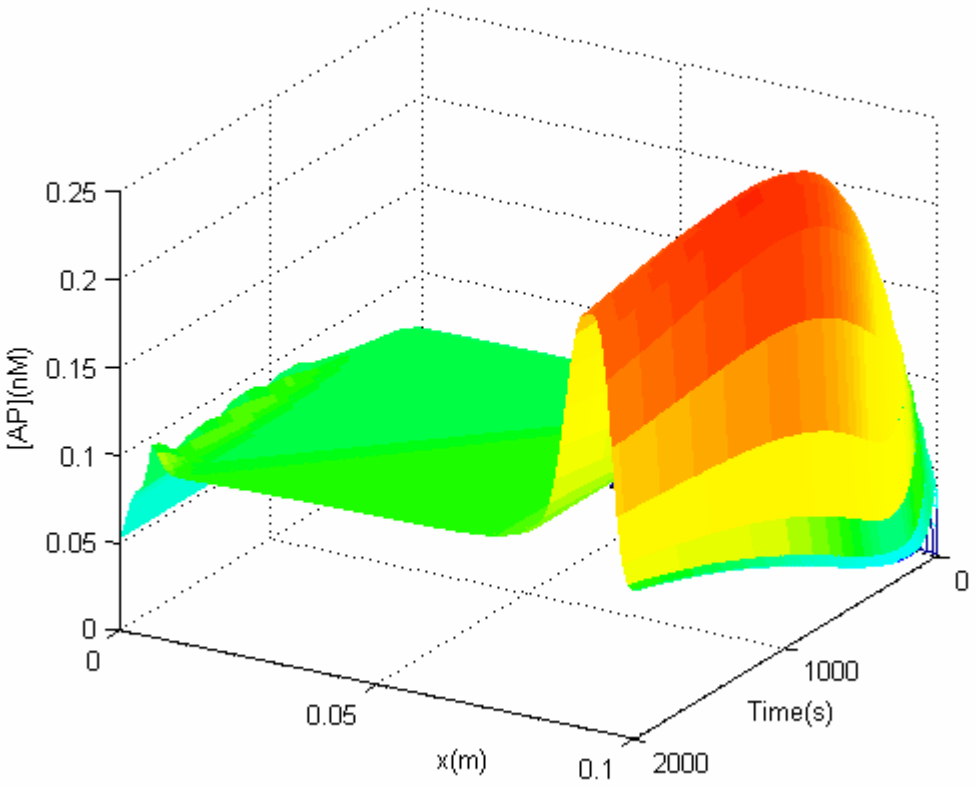

Fig.9: The concentration of the complex AP in the sandwich sedimentation biodetector as a function of space and time. $[A]_0$=10 nM, $[B]_0$=10 nM, and $[P]_0$=1 nM.

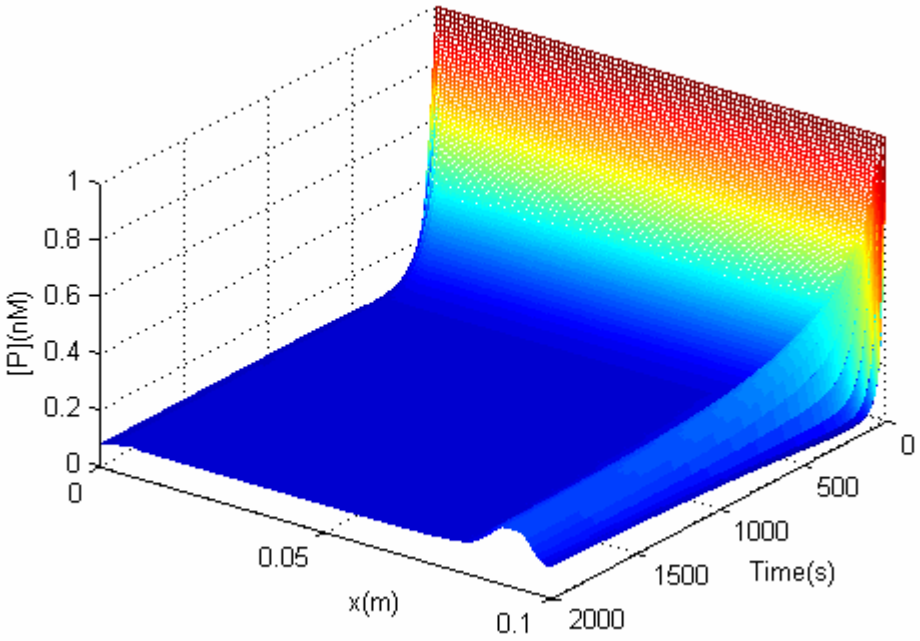

Fig.10: The concentration of the reporter particles P in the sandwich sedimentation biodetector as a function of space and time. $[A]_0$=10 nM, $[B]_0$=10 nM, and $[P]_0$=1 nM.

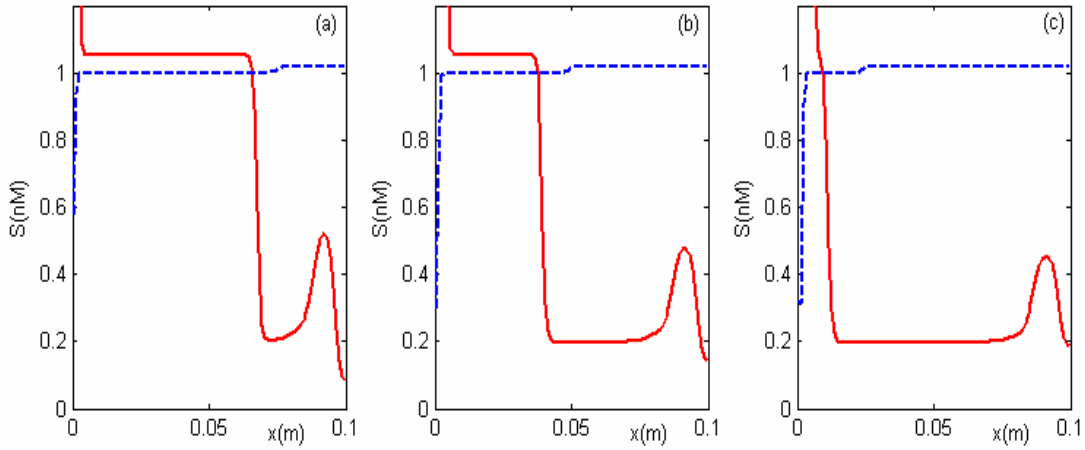

Fig.11: The signal S=[P]+[BP]+[BAP] as a function of *x* at 10 minutes (a), 20 minutes (b), and 30 minutes (c) in the presence of target analyte $[A]_0$=10 nM (solid line) and in the absence of target analyte $[A]_0$=0 nM (dashed line) during the sandwich sedimentation reactor.

Table 1: The material properties of the particle and fluid species involved in the competitive and sandwich formats

	Species	d_i [10^{-6} m]	ρ_i [kg/m^3]	MW_i [kg/mol]
1	Protein-conjugated settling bead B	5.0	5300	1.0×10^{10}
2	Protein-conjugated reporter particle P	0.1	1300	1.07×10^{11}
3	Complex AP	0.1	1300	1.07×10^{11}
4	Complex BP	5.0	5300	1.17×10^{11}
5	Complex BA	5.0	5300	1.0×10^{10}
6	Complex BAP	5.0	5300	1.17×10^{11}
7	Target analyte A	N/A	N/A	150
8	Buffer solution	N/A	1000.	N/A

Table 2: The interaction rate constants of the reactions involved in the competitive and sandwich formats

Interaction	k_a (1/Ms)	k_d (1/s)	Comments
B+A=BA	10^7	10^{-3}	Competitive and sandwich assays
P+A=AP	10^6	10^{-3}	Sandwich assay
B+P=BP	10^6	10^{-3}	Competitive assay
B+AP=BAP	10^7	10^{-3}	Sandwich assay
BA+P=BAP	10^6	10^{-3}	Sandwich assay